Magnetic Pulse Welding and Spot Welding with Improved Coil Efficiency—Application for Dissimilar Welding of Automotive Metal Alloys

Chady Khalil, Surendar Marya and **Guillaume Racineux** *

Research Institute in Civil and Mechanical Engineering (GeM, UMR 6183 CNRS), Ecole Centrale de Nantes, 1 rue de la Noë, F-44321 Nantes, France; chadykhalil@gmail.com (C.K.); surendar.marya@ec-nantes.fr (S.M.)
* Correspondence: guillaume.racineux@ec-nantes.fr

Abstract: Lightweight structures in the automotive and transportation industry are increasingly researched. Multiple materials with tailored properties are integrated into structures via a large spectrum of joining techniques. Welding is a viable solution in mass scale production in an automotive sector still dominated by steels, although hybrid structures involving other materials like aluminum are becoming increasingly important. The welding of dissimilar metals is difficult if not impossible, due to their differential thermo mechanical properties along with the formation of intermetallic compounds, particularly when fusion welding is envisioned. Solid-state welding, as with magnetic pulse welding, is of particular interest due to its short processing cycles. However, electromagnetic pulse welding is constrained by the selection of processing parameters, particularly the coil design and its life cycle. This paper investigates two inductor designs, a linear (I) and O shape, for the joining of sheet metals involving aluminum and steels. The O shape inductor is found to be more efficient both with magnetic pulse (MPW) and magnetic pulse spot welding (MPSW) and offers a better life cycle. Both simulation and experimental mechanical tests are presented to support the effect of inductor design on the process performance.

Keywords: magnetic pulse welding; spot welds; linear coils; shear lap test; automotive alloys; numerical analysis; LS-DYNA

1. Introduction

The emissions targets set by various climate summits, which started in the 1970s, as well as the increase in oil prices since then, has made the automotive OEMs focus their efforts on optimizing vehicle emissions and keeping fuel consumption at a minimum to meet both the environmental and end customers' economic concerns. These efforts were translated by extensively optimizing the combustion engines, introducing the hybrid concept, and introducing, during the 1990s, the first commercial electric vehicles. The common helping factor for all the versions proposed was reducing the weight of the structural and non-structural components by using a combination of materials.

The metal percentage of the materials used in the production of a typical passenger vehicle, even by the year 2025, is expected to maintain a big part of the share: 60% steel (combination of low-carbon, mild-, and high-strength steels), 18% for aluminum, and 5% magnesium [1]. Consequently, the use of these materials implies the need to deal with the challenges related to dissimilar metal joining by overcoming the constraints stemming from unmatching properties (mechanical, thermal, and chemical) and by ensuring manufacturing conditions (limit the damage on joining partners, reliable and cost-efficient processes, and recyclability).

The traditional joining technologies which are well established in the industry are the mechanical and thermal techniques. The former includes processes such as screwing, riveting, punch riveting and clinching.

The main disadvantages of these processes are the additional steps required in the production cycle, stress concentrations at the points of fastening, and weight increase inherent to the fasteners themselves [2,3]. For fusion welding technologies that implicitly involve a heat source with or without a filler addition, the main concern is microstructural changes, residual stresses and defects during the solidification of the molten zone between the adjoining components. For instance, weld fusion zones are not always exempt from porosity, solidification cracks and oriented structures with grain orientations that induce unpredictable variability in the welded components [4,5]. When a filler is additionally used to mitigate weld metal chemistry, the weight increase is inherent, as in mechanical joints. In automotive applications of fusion welding, resistance spot welding has been in practice for a very long time and, for the last two decades, remote laser spot welding is increasingly preferred due to the processing speed [6,7]. Further lightweight automotive body structures imply hybrid materials as diverse as aluminum and steels and need fast joining technologies to keep pace with the large-scale automotive sector [8]. The fusion welding of such dissimilar materials is more complex due to the formation of intermetallic compounds in the weld zone and the presence of differential thermal effects stemming from different physical properties, like the thermal expansion coefficient and melting points. This leads to the unacceptable weakening of the welded components. In the case of aluminum to steel thermal joining application, two important limitations need to be mentioned: the formation of brittle, aluminum, rich-intermetallic compounds (Fe_2Al_5, $FeAl_3$) and the negligible solid solubility of Fe in Al [9]. For a viable dissimilar joint, one possible way of doing this is to reduce, as much as possible, the size of the intermetallic phases. For this to happen, amongst other alternatives to minimize the formation of brittle compounds, some prospective studies involve laser roll bonding through brazing [10] and mixing, as in friction spot welding [11], but with limited success in large-scale applications.

To overcome the mechanical and thermal limitations, the studies of high-velocity impact processes which create a direct joining between metals at solid-state and at microscopic level presented an opportunity. These studies started first in the 1950s with the explosive welding (EXW) [12], and continued with magnetic pulse welding (MPW), laser impact welding (LIW) [13], and vaporizing foil actuator welding (VFAW) [14]. The cold and rapid natures of these processes—some microseconds—limit the risk of HAZ and intermetallic compounds' formation, respectively [15].

The principle of the high-velocity impact processes is based on accelerating one metal, called a flyer, at very high velocities, towards another fixed metal, called parent, where the local progressive collision creates the bond between the two materials. The difference lies in the accelerator types: in EXW, for example, the detonators are used, while in MPW, electromagnetic driving forces are used [2–5]. For safety and ergonomic reasons of massive industrial applications, the MPW process presents itself as a more appropriate candidate, as it uses the electromagnetic fields as a source.

The driving force generation is based on the Laplace force principle: the presence of a current-carrying conductive metal in a time-varying magnetic field generates Laplace forces on this metal. Therefore, and to achieve large amounts of Laplace forces, the MPW processes use:

- A high pulse generator capable of generating an intense, time-varying current that will be the source of the time-varying magnetic field;
- A coil capable of producing the magnetic field due to the discharged current delivered by the generator;
- A conductive metal in the vicinity of the coil in which the magnetic field penetrates and induces currents, leading to the generation of large amounts of Laplace forces, causing its acceleration.

MPW for a tubular geometry was the most used and developed in the MPW field [16,17]. Starting in the year 2000, more focus was given to the sheet metal applications where the operational positioning

is presented in Figure 1a,b and Figure 2A. Manogaran et al. [18] developed an additional process concept for metal sheets: Magnetic Pulse Spot Welding (MPSW). In this process, a prior local stamping is created on the intended spot-welding location in the flyer metal, which is called the hump (Figure 1c,d); this hump will guarantee the required standoff distance, and hence the flyer could be directly placed on the parent metal without any concern for the overlapping distance between the two materials to comply with the industrial ease for automated applications. This hump will then be accelerated by the magnetic pulse to create a spot weld after collision (Figure 2B).

After this brief description of the MPW/MPSW, the process's operational parameters can be concluded: the electrical coil's geometry, the configuration's geometrical parameters and the discharge energy of the generator. These operational parameters condition the collision mechanism, where the two impact physical parameters are the impact velocity and the impact angle, which are mandatory to ensure two clean surfaces ready for welding and the formation of the jet [2–6,19].

It is worth mentioning that the impact would invariably generate heat by the transformation from mechanical to thermal energy, thereby limiting the highest impact velocity that would not engender melting at the welded interface. For dissimilar joints, as mentioned earlier, melting has to be curtailed in order to eliminate the possible formation of intermetallic compounds. It is worth noting that, due to short impact times, heat generation remains nearly adiabatic and localized in the interfacial zone. In the case of Al to Cu impact joining, Marya et al. [20] have reported localized melting in tube to tube welding, which has been substantiated by others [15,19]. Briefly, the velocity range for successful welding has a limited window and consequently an equal choice of parameters like standoff distance, discharge energy and configuration of sheets/parts.
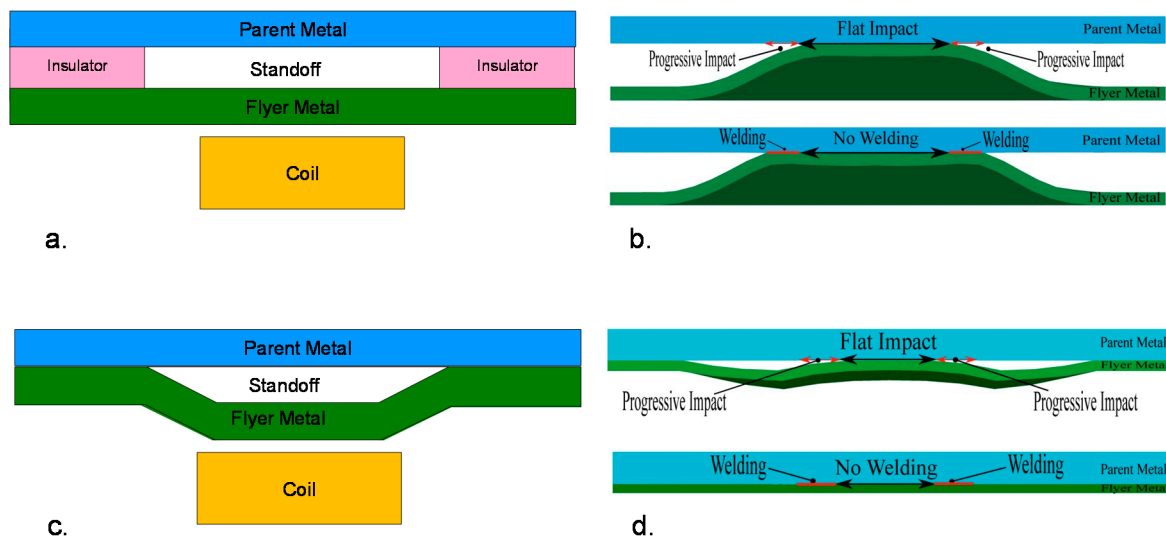

Figure 1. (**a**,**b**) Magnetic Pulse Welding (MPW); (**c**,**d**) Magnetic Pulse Spot Welding (MPSW).

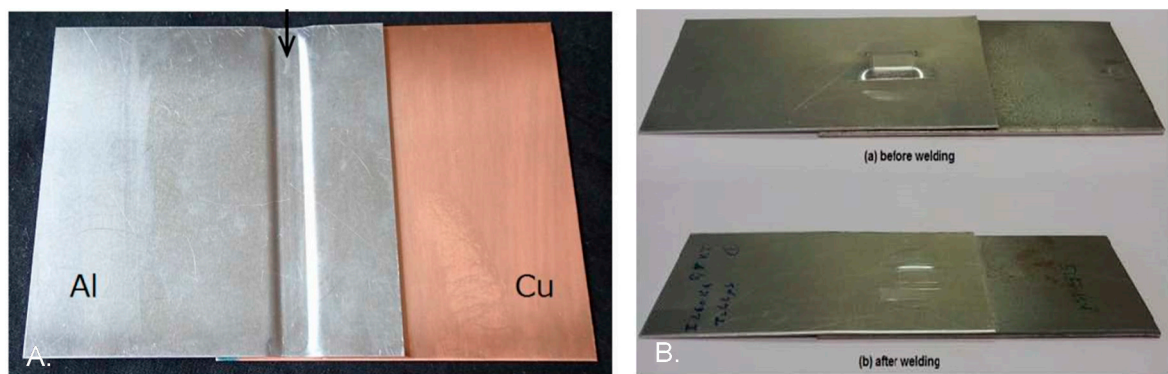**Figure 2.** (**A**) Al/Cu MPW [21]; (**B**) MPSW [18].

Objectives of Study

The MPW/MPSW for sheet metal applications has been successfully applied and achieved for similar and dissimilar metals welding [1,4,7–10,22]: aluminum to aluminum, aluminum to steel, aluminum to magnesium. In the literature, a lot of alloys were tested, and the applications, in general, concerned thin sheet metal thicknesses, omitting the real thicker sheets that can be applied in real applications for the automotive industry. On the other hand, the most used electrical coil during these studies were linear with rectangular cross-section coils, which present a good efficiency to simplicity ratio for aluminum 1xxx and thin sheet applications [1,11].

However, in automotive applications, the 5000- and 6000- series aluminum alloys' use is dominant (body panels, seat structures, reinforcement members, etc.). On the steel side, the low-carbon drawing steels are used for various components and, during the last three decades, the developments of the advanced high-strength steels (AHSS) led to the increase in the use of the dual phase steels (DP) [23].

In this context, the current study aimed to develop an electrical coil geometry allowing a better efficiency and wider application scope of the MPW/MPSW for the automotive metal alloys. The new geometry coils, as will be seen in the results, led to a wide range of successful welds for different combinations of similar and dissimilar alloys. Several combinations were also tested under quasi-static, dynamic and fatigue loads to see the welds strengths level.

First, the equipment used, including the two coils (linear and the newly designed), the experimental setup (Figure 3) and an LS-Dyna numerical model which will be used in the analysis of the improved efficiency of the new coil design, will be presented. After that, we will present the comparison of the two coils and proceed to the experimental results.
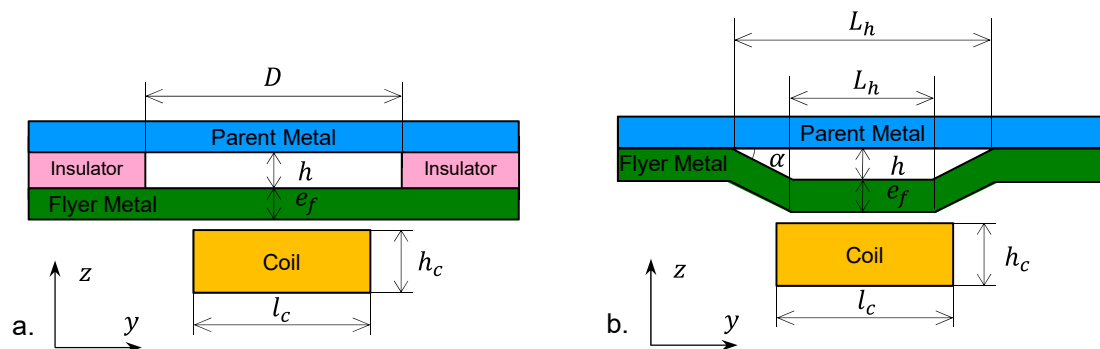

Figure 3. Experimental setup: (**a**) MPW; (**b**) MPSW.

2. Materials and Methods

2.1. Materials

The aluminum and steel alloys chemical compositions used during this study are presented in Tables 1–3. Their mechanical properties are given in Tables 4 and 5.

Table 1. Aluminum alloys, chemical compositions (%at.).

	Si max	Fe max	Cu max	Mn max	Mg max	Cr max	Zn max	Ti max	Other max
1050	0.25	0.40	0.05	0.05	0.05	-	0.07	0.05	0.03
5182	0.20	0.35	0.15	0.50	4.0–5.00	0.10	0.25	0.10	0.15
5754	0.40	0.40	0.10	0.50	2.6–3.6	0.30	0.20	0.15	-
6013	0.78	0.28	0.97	0.40	1.02	0.06	0.10	0.05	0.15
6016	0.5–1.5	0.50	0.20	0.20	0.25–0.70	0.10	0.20	0.15	0.15

Table 2. DC04 steel chemical compositions (%at.).

	C max	Mn max	Si max	P max	S max	Al max
DC04	0.08	0.40	0.10	0.025	0.025	0.020

Table 3. DP steels chemical compositions (%at.).

	C max	Mn max	Si max	P max	S max	Al max	Ti + Nb max	V max	Cr max	Mo max	B max	N max	Ni max	Nb max
DP450	0.10	0.16	0.4	0.04	0.015	0.015–0.08	0.05	0.01	0.8	0.3	0.005	0.008	-	-
DP1000	0.139	1.50	0.21	0.009	0.002	0.046	-	0.01	0.02	-	0.0002	0.003	0.03	0.015

Table 4. Steel's mechanical properties.

	YS (MPa)	UTS (MPa)	A % ISO 20 × 80
DC04 (*e* ≤ 1.47 mm)	160–200	280–340	37
DP450	290–340	460–560	27
DP1000	787	1059	8.5

Table 5. Aluminum alloys' mechanical properties.

	YS (MPa)	UTS (MPa)	A % ISO 20 × 80
1050-H14	85	105	4
5754-H111 (*e* ≤ 1.5 mm)	90–130	200–240	21
5182 (*e* ≤ 1.5 mm)	120–160	260–310	23
6013-T4	174	310	26
6016-T4	110–150	220–270	23

2.2. Equipment and Experimental Procedure

2.2.1. Pulse Generator

The pulse generator used is a 50 kJ, developed at ECN, with the following characteristics:

$$C_{Gen} = 408 \text{ µF, } L_{Gen} = 0.1 \text{ µH; } R_{Gen} = 3 \text{ mΩ; } V_{max} = 15 \text{ kV; } I_{max} = 500 \text{ kA; } f_{short} = 25 \text{ kHz.}$$

The highest limit for the discharge energy is hence fixed at 16 kJ, so that the discharge current does not exceed 80% of the maximum allowable current for the generator:

$$I_{operation_{max}} = 0.8 \times I_{max} = 400 \text{ kA}$$

2.2.2. Coils

The two coils used in this study are a linear rectangular cross-section coil—dimensions are presented in Figure 4—and an O-shaped rectangular cross-section coil—dimensions are presented in Figure 5. The active areas of the two coils are the same: 20 × 8 mm.

2.2.3. Discharge Energy and Discharge Current Relation

The discharge energy *E* depends on the voltage that is charging the capacitors and it can be expressed by

$$E_{discharge} = \frac{1}{2} C_{Gen} V_0^2 \tag{1}$$

where C_{Gen} is the generator capacitance and V_0 is the charging voltage.

The resulting discharge current in the coil, which is highly damped sinusoidal due to the RLC equivalence of the circuit, is

$$I(t) = I_0 e^{-\frac{t}{\tau}} \sin(\omega t) \tag{2}$$

where

$$I_0 = V_0 \sqrt{\frac{C_{Gen}}{L}} \tag{3}$$

$$\tau = \frac{2L}{R} \tag{4}$$

$$\omega = \frac{1}{\sqrt{LC_{Gen}}} = \frac{f}{2\pi} \tag{5}$$

with L and R as the equivalent inductance and resistance of the system, respectively

$$L = L_{Gen} + L_{Coil} \tag{6}$$
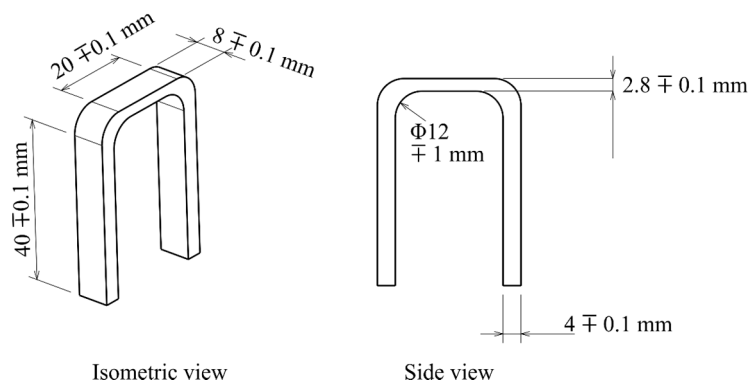
$$R = R_{Gen} + R_{Coil} \tag{7}$$

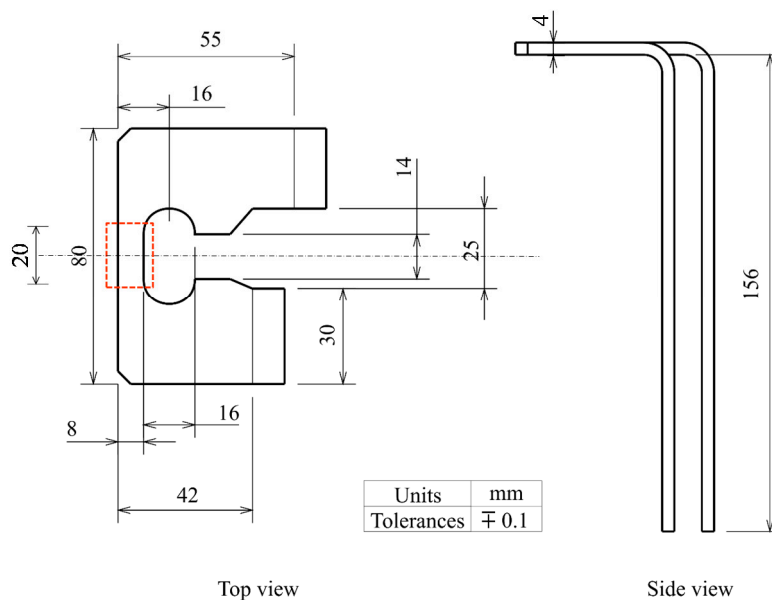**Figure 4.** Linear rectangular cross-section coil.

Figure 5. O-shape coil dimensions.

2.2.4. Experimental Procedure and Design

In the case of the MPW (Figure 1a,b), the configuration involves the use of insulators to create the needed airgap between the two metals (Figure 3). The insulators are made of PE and PVC and they are

designed to have the same thickness of the required standoff distance between metals. They are fixed on the flyer metal using adhesive tapes. In Figures 6 and 7, the positioning of the flyer metal regarding the coil is represented for both linear and O-shaped coils, respectively.
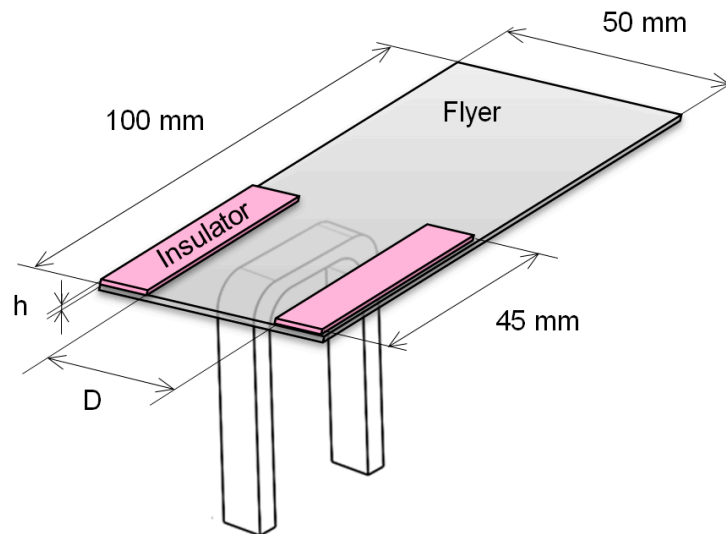

Figure 6. Magnetic Pulse Welding configuration with linear coil.
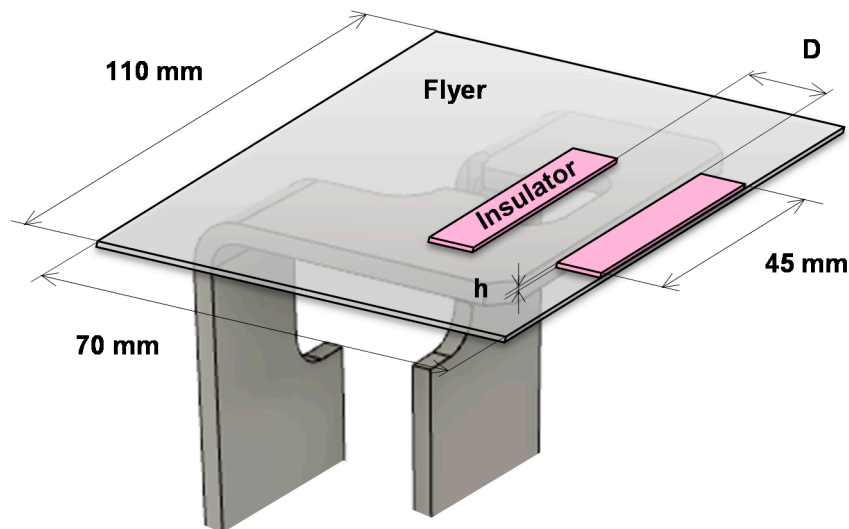

Figure 7. Magnetic Pulse Welding configuration with O-shape geometry coil.

After the cleaning step, the flyer metal is positioned facing the coil where a Kapton insulation sheet with a 0.1 mm thickness is used to separate it from the coil. The positioning is controlled by a laser so that the part of the flyer metal to be deformed is centered regarding the coil's active area. The parent metal is then positioned on the insulators, over it a massive steel die, and finally the whole system is clamped using a special system designed to avoid any displacement during the welding process. The standoff distance is controlled using a feeler gauge before every test.

In case of MPSW (Figure 1c,d and Figure 3b), the first step of the process is to create the hump in the flyer metal. The general geometry of the hump chosen is a rectangular one. This geometry was chosen based on the previous study done by Manogaran et al. [19], during which different geometries were tested, and it was proven that the rectangular one is the more efficient. Figure 8 presents this general geometry with different dimensions. The hump is stamped in the flyer metal using a hydraulic press die.
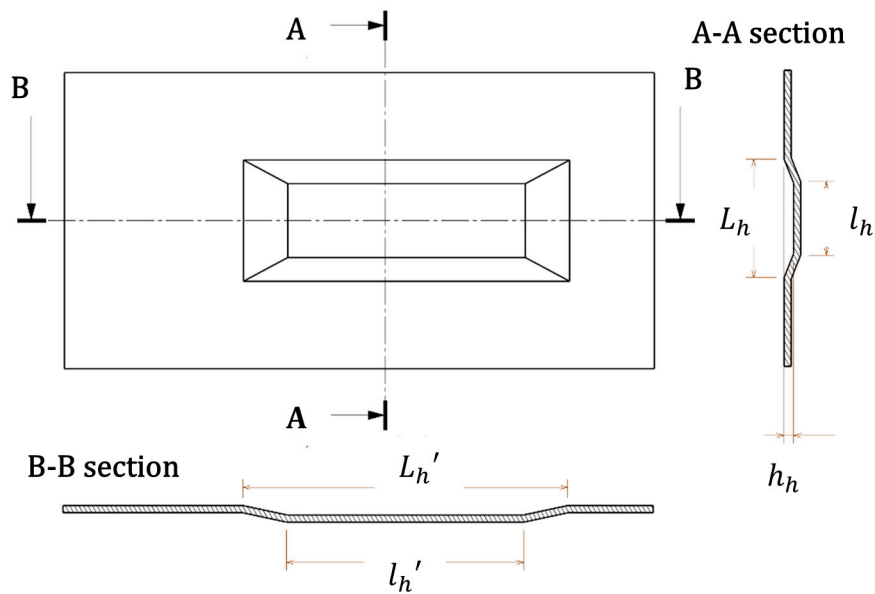
Figure 8. General geometry of the hump for MPSW.

After cleaning the metal surfaces from oil using acetone solution, the flyer metal is then positioned with a laser so that it is facing and centered on the coil's active area. The parent metal is then positioned above the flyer metal with the massive die on, and finally the system is clamped like the MPW case.

2.2.5. Welds Strength Evaluation

For the welding mechanical strength evaluation, the welded specimens were tested as schematically represented in Figure 9 in lap-shear conditions:

- Quasi-static at 10^{-2} mm/s (with an Instron 5584 mechanical tensile machine, Norwood, MA, USA);
- Dynamic at 614 mm/s (with an MTS 819 hydraulic high-speed tensile machine, Eden Prairie, MN, USA);
- Fatigue under unidirectional conditions ($R = 0$, frequency of 20 Hz, $F_{max} = 0.6 \times F_{\mathrm{max}quasi-static}$ with an MTS Electropulse E10000 machine, Eden Prairie, MN, USA).
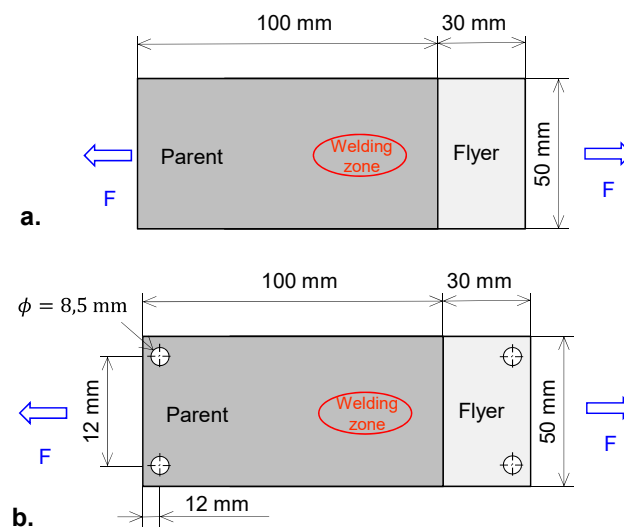

Figure 9. (**a**) quasi static and fatigue lap shear tests specimen, (**b**) dynamic lap-shear test specimen.

2.2.6. Numerical Simulation

The model used is a coupled mechanical/thermal/electromagnetic using LS-DYNA 3D FEM-BEM code (Finite Element Method – Boundary Element Method).

The simulations during this study were performed using the High-Performance Computing (HPC) resources of the Centrale Nantes Supercomputing Center on the cluster Liger by the High-Performance Computing Institute (ICI).

2.3. Materials Properties and Boundary Conditions

The coils material used in this study are the OFHC copper and the ASTM A36 steel. The flyer metals used in the numerical models are the aluminum alloys 5754 and 5182. The parent metal is the DC04 deep drawing law carbon steel.

A Johnson–Cook model was used for the mechanical solver and the parameters for all materials are taken from the literature [24–27] and they are presented in Table 6. The thermal and electrical parameters of different materials are presented in Tables 7 and 8 and they are also taken from the literature [24–27]. The initial room temperature T_{RT} was set at 293 K.

Table 6. Johnson–Cook model parameters.

Coil	Alloy	A (MPa)	B (MPa)	n	C	m
Linear Coil	OFHC	90	292	0.31	0.025	1.09
O-Shape	OFHC	90	292	0.31	0.025	1.09
Coil	ASTM A36	286.1	500.1	0.2282	0.022	0.917
Flyers	5754	67.456	471.242	0.424	0.003	2.519
	5182	106.737	569.120	0.485	−0.001	3.261
Parent	DC04	162	598	0.6	2.623	0.009

Table 7. Thermal properties.

Coil	Alloy	Thermal Conductivity (W/mk)	Specific Heat Capacity (J/kgK)
Linear Coil	OFHC	386	383
O-Shape Coil	OFHC	386	383
	ASTM A36	50	450
Flyers	5754	130	897
	5182	123	902
Parent	DC04	52	470

Table 8. Electrical Properties—International Annealed Copper Standard.

Coil	Alloy	%IACS (International Annealed Copper Standard)	S/m
Linear Coil	OFHC	100	5.8001×10^7
O-Shape Coil	OFHC	100	5.8001×10^7
	ASTM A36	12	6.9600×10^6
Flyers	5754	33	1.9140×10^7
	5182	28	1.6240×10^7
Parent	DC04	13	7.5400×10^6

The variation in the electrical conductivity, with temperature for the copper and aluminum, is based on the Meadon model, which is a simplified Burgess model [28], and it gives the conductivity as a function of temperature and density at solid phase [29]

$$\rho = \left(C_1 + C_2 T^{C_3}\right) f_c\left(\frac{V}{V_0}\right) \tag{8}$$

where ρ is the electrical resistivity, T is the temperature, V is the specific volume, V_0 is the reference specific volume (zero pressure, solid phase) and

$$f_C\left(\frac{V}{V_0}\right) = \left(\frac{V}{V_0}\right)^{2\gamma-1} \tag{9}$$

where γ is the Gruneisen value given by

$$\gamma = \gamma_0 - \left(\gamma_0 - \frac{1}{2}\right)\left(1 - \frac{V}{V_0}\right) \tag{10}$$

with γ_0 the reference Gruneisen value. In Table 9, the set of parameters for aluminum and copper from Burgess paper are given [20,21].

Table 9. Meadon-Burges parameters.

Parameter	Cu	Al
V_0 (cm^3/g)	0.112	0.370
γ_0	2	2.13
C_1	-4.12×10^{-5}	-5.35×10^{-5}
C_2	0.113	0.223
C_3	1.145	1.210

For the steel case, a simple linear model was used

$$\rho = \rho_0[1 + \alpha_0(T - T_{RT})] \tag{11}$$

where ρ is the electrical resistivity at the actual temperature T, ρ_0 is the electrical resistivity at the reference temperature T_{RT} and $\alpha_0 = 6 \times 10^{-3}$ K^{-1} is the temperature coefficient of resistivity for the taken T_{RT} reference temperature.

The source currents in the coil are due to the imposition of boundary conditions, where it is possible to have an imposed current or an imposed voltage [29]. In our case, the voltage $V(t)$ is imposed through an equation depending on the charging voltage V_0, the resistance R_{Gen}, the inductance L_{Gen} and capacity C_{Gen} of the generator, as well as the mesh resistance and inductance (Figure 10). Dirichlet and Newman boundary conditions are applied, and no further constraint is applied on the BEM [30].
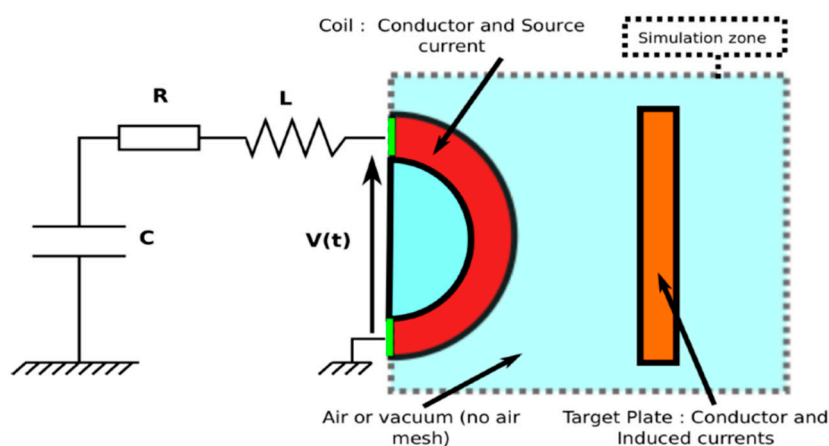

Figure 10. Problem with (R, L, C) imposed voltage on the coil [28].

The inductor nodes' movement was constrained in all directions (translation and rotation), since in the MPW applications, the coils are fixed in such a way as to prevent their movement. It is the same

for the parent metal nodes. The flyer sheet nodes' movement in MPW overlapping case (Figure 11) was blocked outside the distance that represents the distance between the insulators. In the case of the MPSW (Figure 12), and since the hump is the only part that will be accelerated from the flyer, all the other nodes were also constrained.
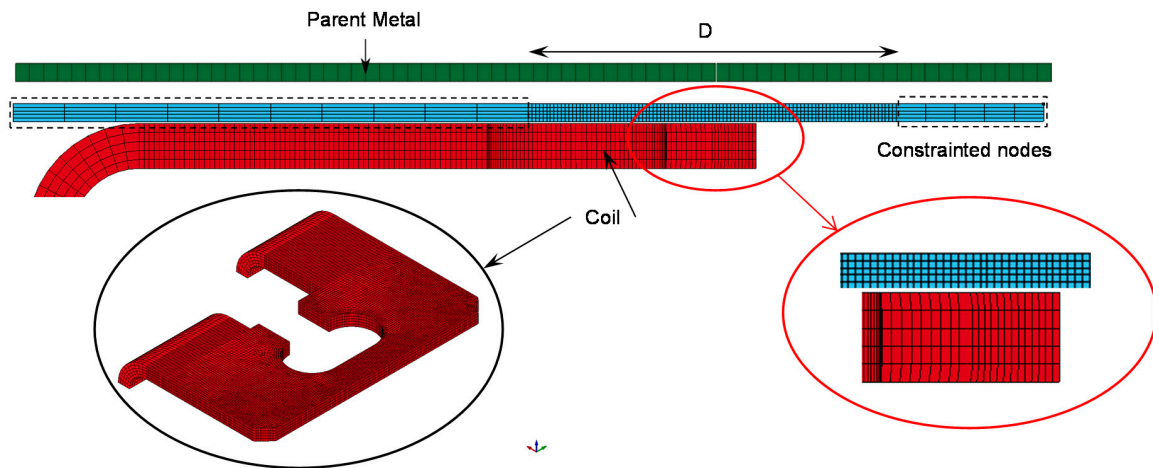

Figure 11. Model in the MPW overlapping configuration with O shape coil.
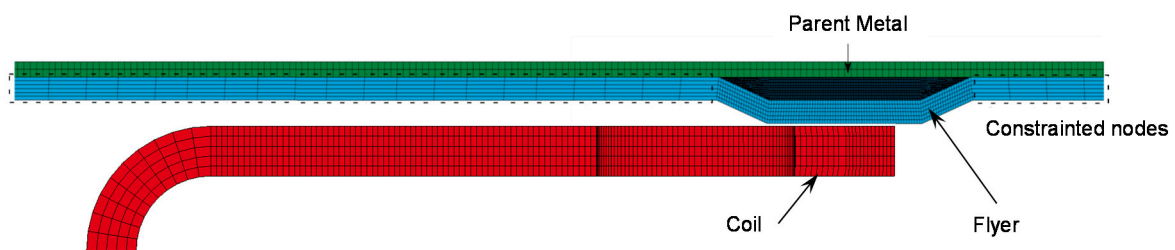

Figure 12. Model cross section view in the MPSW configuration with O shape coil.

2.4. Mesh and Time Step

The electromagnetic solver uses eight nodes' brick elements only, and hence the mesh was controlled to not have any other type of elements in the model. Since we are in a 3D full-coupled simulation, and to avoid very long simulation times, the length of one element edge l_e in the non-active zones was equal to the skin depth δ, and in the active zones it was smaller to have accurate numerical results:

$$l_e = \frac{\delta}{3} \tag{12}$$

The time-step Δt for the electromagnetic solver is computed as the minimal elemental diffusion time step over the elements [30]

$$\Delta t = \frac{\mu_0 \sigma}{2} \, l_e{}^2 \tag{13}$$

where μ_0 is the magnetic permeability of the material and σ its electrical conductivity.

3. Results and Discussion

3.1. Numerical Comparison of Linear and O-Shape Coils Efficiencies

The presence of a current-carrying conductive metal in a time-varying magnetic field generates Laplace forces on this metal. The Laplace force acting on an elementary volume dV is expressed in (14). In the MPW case, the flyer metal is the current-carrying conductive where the mentioned current is induced due to the time-varying magnetic field generated by the discharged current in the coil. Consequently, and in accordance with the following Equation (14),

$$d\vec{F} = \vec{J} \times \vec{B} \, dV \tag{14}$$

The forces generated are directly proportional to the induced current density in the flyer metal and the magnetic induction generated by the discharge current, which are also related, since the latter is the source of the former.

Going back to the Laplace force equation, the O-shape coil design presented in Figure 13 is based on the idea of improving efficiency by having higher discharge currents and induced currents at the same levels of energies based on:

- Reducing the inductance of the coil to increase the peak currents (3);
- Putting more charge carriers on the flyer metal in movement to increase the induced currents magnitude and increasing, at the same time, the current density in the area where the material should be accelerated.
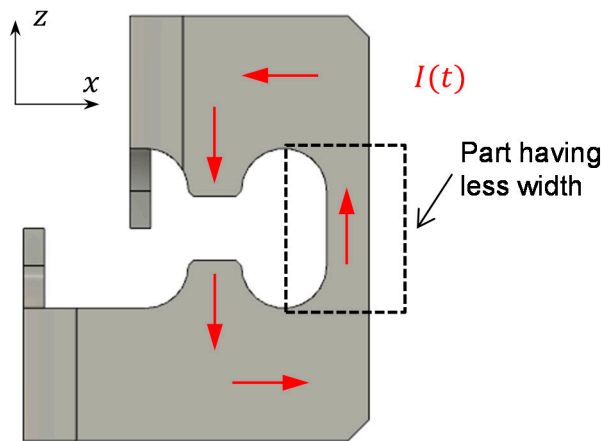

Figure 13. O-Shape rectangular cross-section.

The measured inductance of the linear coil presented a value equal to 81% of the generator's inductance L_{Gen}, giving a system total inductance of

$$L_1 = 1.81 L_{Gen} \tag{15}$$

The measured inductance of the O-shape coil presented a value equal to 49% of the generator's inductance L_{Gen}, giving a system total inductance of

$$L_2 = 1.49 L_{Gen} \tag{16}$$

Comparing the inductances, the system with the O-shape had a 10% higher peak current and frequency.

$$L_2 = 0.82 L_1 \tag{17}$$

$$\frac{I_{02}}{I_{01}} = \frac{\omega_2}{\omega_1} = 1.1 \tag{18}$$

To compare the efficiency of the O-shape vs. the linear coil, the developed numerical model was used to compare the flyer velocities in the MPW configuration case for the thick aluminum 5754-H111 ($e_f = 1.2$ mm). Since the discharge currents are higher in the O-shape coil case, the mechanical strength of the coil should be higher, and hence two approaches were considered. In the first, the material of the coil is kept as OFHC copper, but the thickness was increased to 4 mm (i.e., 1.4 times the thickness in the linear coil case). The second approach involves the use of a 4-mm thickness coil made of steel ASTM

A36, which has better mechanical properties, and seeing whether the loss in electrical conductivity will have a high influence on its global efficiency.

Figure 14 presents a comparison between impact velocities for the cases of use of an OFHC copper O-shape and a linear OFHC copper coil. The velocities at $E = 10$ kJ in the O-shape coil case are much higher than these at $E = 16$ kJ in the linear case. The velocity in the O-shape case is, on average, 1.75 times the velocity in the linear coil shape.

When using a steel O-shape coil, the velocities are 1.55 times the velocities in the linear coil case. The velocities' curves at different standoff distances in both cases are presented in Figure 15.

The data presented in Figures 14 and 15 show clearly that the O-shaped coil is far better than the linear coil and, even when steel is used for the coil, it still has higher efficiency than the linear coil.
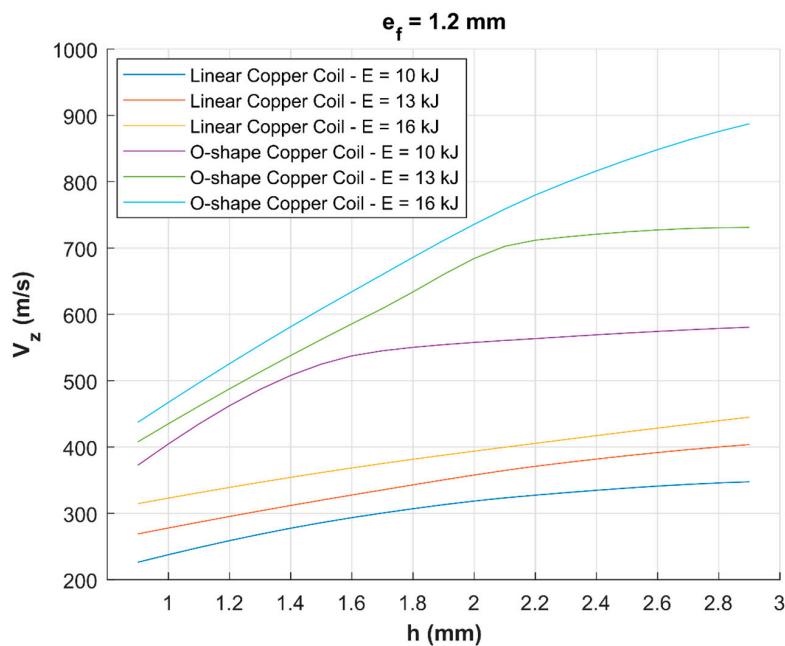

Figure 14. Impact velocity comparison between the OFHC O-shape and linear coils ($e_f = 1.2$ mm).
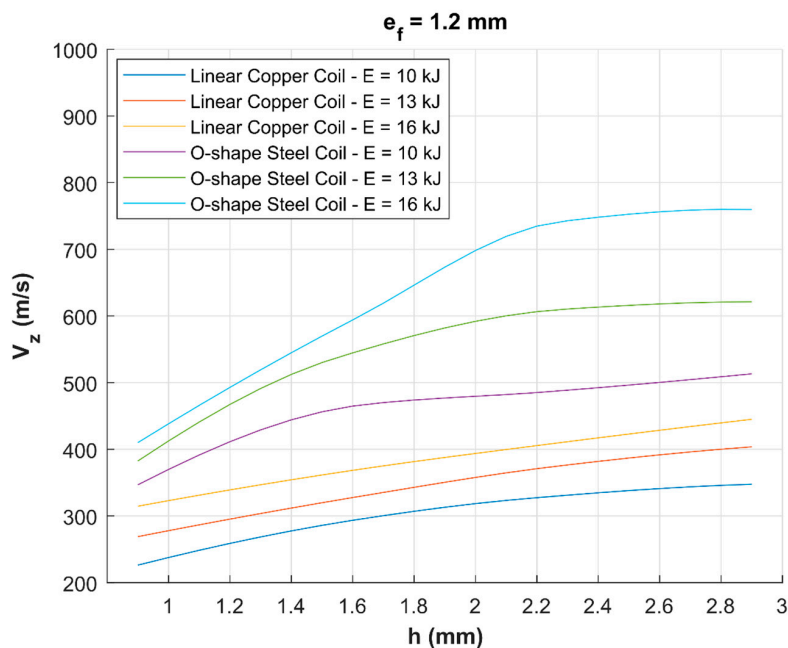

Figure 15. Impact velocities comparison between the steel O-shape coil and linear copper coil ($e_f = 1.2$ mm).

3.2. Experimental Validation

The first step in the experimental analysis was to explore the weldability between various metal sheets with various mechanical properties and thicknesses, using both coils in the same range of discharge energies (4 kJ ≤ $E_{discharge}$ ≤16 kJ). The configuration used is the MPSW and the hump dimensions (Figure 8) are: l_h = 8 mm; L_h = 12 mm; l'_h = 10 mm, L'_h = 18 mm, and h_h = 1.6 mm.

Table 10 summarizes the results for different combinations. The limit of the linear coil can be observed when flyer metal thickness exceeds 1.2 mm, while the O-shape coil succeeded the welds up to 2 mm.

Table 10. Weldability of different metals alloys using copper linear coil (L) and O shape coil (✗: not welded/✓: welded/-: not tested).

Parent Flyer	5754		5182		6016		DP450		DP1000		DC04	
	L	O	L	O	L	O	L	O	L	O	L	O
5754 (0.5 mm)	✓	✓	✓	✓	✓	✓	✓	✓	✓	✓	✓	✓
5182 (1 mm)	✓	✓	-	-	-	-	✓	✓	-	-	✓	✓
5182 (1.2 mm)	✓	✓	-	-	-	-	✓	✓	-	-	✓	✓
5182 (1.4 mm)	✗	✓	-	-	-	-	✗	✓	-	-	✗	✓
5182 (2 mm)	✗	✓	-	-	-	-	✗	✓	-	-	✗	✓
6013 (1.4 mm)	-	-	-	-	-	-	-	-	✗	✓	✗	✓
6016 (1 mm)	✓	✓	-	-	-	-	-	-	-	-	✓	✓

3.3. Mechanical Testing for the Welding Joints

Now that the weldability of a variety of combinations is proven using the O-shape coil for thick metal sheets, the strength of welds will be tested. As the focus is the dissimilar welding for automotive applications, five combinations are tested in quasi-static, dynamic, and fatigue lap-shear configuration:

- Aluminum 5182 (e_f = 1.2 mm) with steel DC04 (e_p = 0.8 mm) in MPSW configuration;
- Aluminum 6016 (e_f = 1 mm) with steel DC04 (e_p = 0.8 mm) in MPSW configuration;
- Aluminum 5182 (e_f = 1.2 mm) with steel DP450 (e_p = 1.17 mm) in MPSW configuration;
- Aluminum 6013-T4 (e_f = 1.4 mm) with steel DP1000 (e_p = 1 mm) in MPSW configuration;
- Aluminum 6013-T4 (e_f = 1.4 mm) with steel DP1000 (e_p = 1 mm) in MPW configuration.

For the five combinations, the same steel O-shape coil and the same discharge energy ($E_{discharge}$ = 16 kJ) are used.

For the MPSW configurations, the same hump dimensions are used: l_h = 12 mm; L_h = 20 mm; l'_h = 40 mm, L'_h = 55 mm, and h_h = 1.6 mm.

For the MPW configuration, the distance between insulators is D =18 mm and the standoff distance is h = 1.4 mm.

In each case, three specimens are tested, and the results are presented in Table 11 for quasi-static lap-shear tests, in Table 12 for dynamic lap-shear tests and in Table 13 for fatigue tests.

For 6016/XES dynamic tests, the failure occurred at the aluminum fixation holes at 9000 N without any failure in the welding for all the tested specimens.

The 5182/DC04 weld shows, in the quasi-static lap shear tests, maximum loads between 6250 and 6750 N, with a displacement between 1.62 and 1.7 mm. The failure was in the weld and a deformation of the steel in the welding area was observed. The maximum dynamic loads that the weld attained were between 7900 and 8300 N, with a displacement between 1.38 and 1.53 mm, and the failure occurred in the welding also. Finally, the number of cycles reached during the fatigue tests was between 25,000 and 28,000 cycles, where a tearing is observed in both aluminum and steel plates during the test (Figure 16).

5182/DP450 weld shows in the quasi-static lap shear tests maximum loads between 9200 and 10,000 N and the displacements are between 1.32 and 1.88 mm. The failure occurred in the welds in all

the 3 tests. The maximum dynamic loads were between 6100 and 8500 N and the displacements were between 1.36 and 2.9 mm. The fatigue tests showed that the number of cycles is between 21,000 cycles and 24,000 cycles.

Table 11. Quasi-static lap-shear tests

Materials (Flyer/Target)	Welding Configuration	Fmax—Quasi-Static Lap-Shear Test							
		Average	Average	Specimen 1		Specimen 2		Specimen 3	
		F_{max} (N)	ΔL_{max} (mm)	F_{max} (N)	ΔL_{max} (mm)	F_{max} (N)	ΔL_{max} (mm)	F_{max} (N)	ΔL_{max} (mm)
5182/DC04	MPSW	**6500**	**1.63**	6250	1.56	6500	1.7	6750	1.62
5182/DP450	MPSW	**9400**	**1.64**	10,000	1.88	9000	1.32	9200	1.73
6016/DC04	MPSW	**8433**	**2.15**	8500	2.15	8700	2.3	8100	2
6013/DP1000	MPSW	**7800**	**0.98**	8400	1.1	7600	1.06	7400	0.77
6013/DP1000	MPW	**8767**	**0.98**	9500	1.1	9200	0.95	7600	0.9

Table 12. Dynamic lap-shear tests.

Materials (Flyer/Target)	Welding Configuration	Fmax—Dynamic Lap-Shear Test (0.614 m/s)							
		Average	Average	Specimen 1		Specimen 2		Specimen 3	
		F_{max} (N)	ΔL_{max} (mm)	F_{max} (N)	ΔL_{max} (mm)	F_{max} (N)	ΔL_{max} (mm)	F_{max} (N)	ΔL_{max} (mm)
5182/DC04	MPSW	**8067**	**1.46**	8300	1.48	7900	1.53	8000	1.38
5182/DP450	MPSW	**7033**	**1.88**	8500	2.9	6500	1.37	6100	1.36
6016/DC04	MPSW	**>9000**		>9000		>9000		>9000	
6013/DP1000	MPSW	**7667**	**3.85**	9300	2.75	7400	3.6	6300	5.2
6013/DP1000	MPW	**14,233**	**1.7**	14,600	2.32	14,400	1.3	13,700	0.78

Table 13. Fatigue tests results (R = 0; f = 20 Hz).

Materials (Flyer/Target)	Welding Configuration	F_{max} (kN)	Number of Cycles			
			Average	Specimen 1	Specimen 2	Specimen 3
5182/DC04	MPSW	4	**26,333**	26,000	28,000	25,000
5182/DP450	MPSW	5	**22,333**	21,000	24,000	22,000
6016/DC04	MPSW	4.4	**43,000**	44,000	42,000	43,000
6013/DP1000	MPSW	4.4	**31,000**	32,000	30,000	31,000
6013/DP1000	MPW	5	**64,333**	61,000	69,000	63,000

6016/DC04 weld shows in the quasi-static lap shear tests maximum loads between 8100 N and 8700 N and the displacements are between 2 mm and 2.3 mm. The fatigue tests showed number of cycles between 42,000 and 44,000 and tearing was observed in both aluminum and steel sheets (Figure 17). Concerning the dynamic test in this case and for all tested specimens the failure occurred at the aluminum fixation holes at 9000 N without any failure in the welding.

6013/DP1000 welds were tested in both MPW and MPSW configurations.

- In MPW case: the welds showed quasi-static maximum loads between 7600 and 9500 N with displacements between 0.9 and 1.1 mm. The dynamic loads are between 13,700 and 14,600 N and the corresponding displacements are between 0.78 and 2.32 mm. The fatigue tests showed the number of cycles oscillating between 61,000 and 69,000;
- In the MPSW case: the welds showed quasi-static maximum loads in this case were between 7400 and 8400 N and the displacements were between 0.77 and 1.1mm. The dynamic loads attained were between 6300 and 9300 N and the displacements were between 2.75 and 5.2 mm. The fatigue tests showed a number of cycles between 30,000 and 32,000.
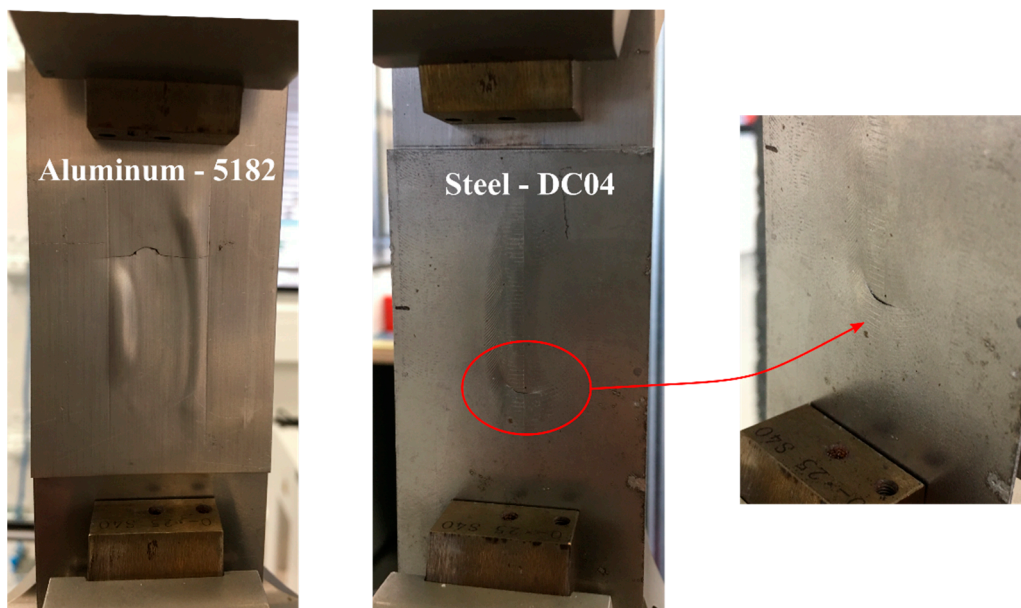
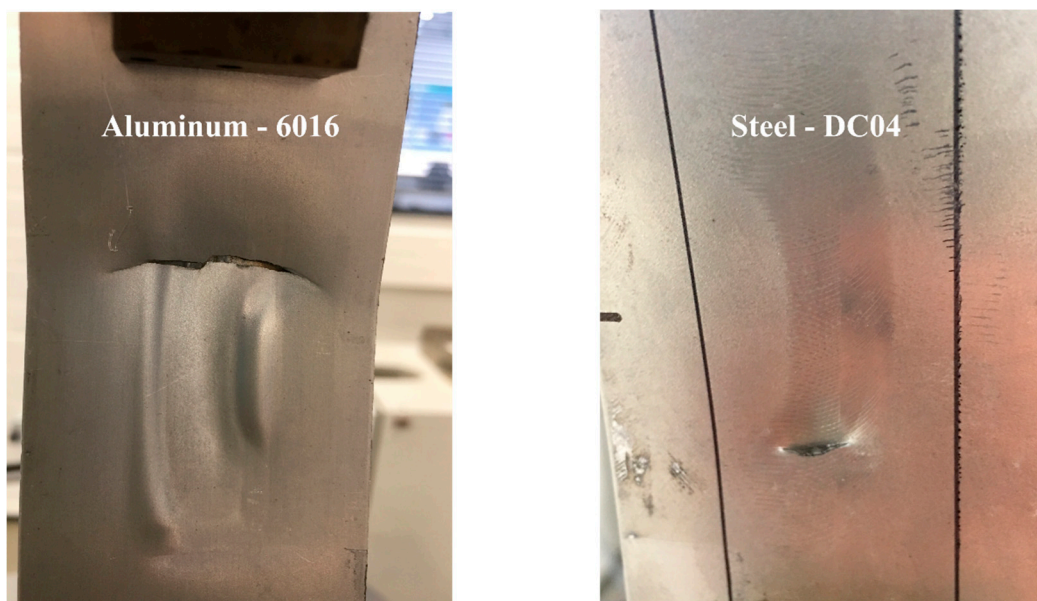**Figure 16.** Aluminum 5182 and steel DC04 tearing during fatigue tests.

Figure 17. Aluminum 6016 and steel DC04 tearing during fatigue tests.

3.4. Inductor Life Cycle

For heavy duty applications prevalent in automotive industry, the inductor must be capable of sustaining repeated shocks during impulse welding. As mentioned earlier in Section 3, the acceleration was imparted to the flyer metal to produce impact velocities, particularly in the case of hard materials and/or thicker sections, which requires either increasing the discharge current and/or reducing the coil cross-section. Subsequently, the coil will then itself experiment higher thermo-mechanical stresses because of the action–interaction properties of the magnetic forces and the significant temperature increase due to Joule effects. The result will be a faster failure of the coil with increasing discharge energies (Figure 18a) for a linear coil. As previously mentioned, O-shape coils provide higher impact velocities compared to straight coil, but what about the life cycle? Table 14 presents the matrix of tests with different inductors and provides information on the cumulative sustainable and average energy/shot. The data analysis gives some trends with discharge energy and coil shape:

- For a straight conductor, the life cycle is drastically reduced from 50 to 10 shots when the discharge energy is increased from 13 to 16 kJ;
- For O-shape conductors, 50 shots with a discharge energy of 18 kJ are observed. This is the highest limit, but with decreasing discharge energy, a much higher number of weld shots could be seen, but this was not evaluated in real terms.

An additional factor is the coil mounting system that has to maintain the inductor in place by counteracting the magnetic forces experimented by coil due to the action–reaction nature during repeated shocks. The magnetic forces occur not only between flyer and coil, but also within the internal parts of the coil itself. This is explicit in Table 14, which shows the effect of a strong coil hold (polyurethane, Figure 18b or by fiberglass/epoxy resin Figure 1c). As a general observation, polyurethane mount leads to coil distortion after a small number of shots (about five shots), while fiber glass/resin hold composite shows only joule heating (50 shots).

Table 14. Matrix of tests with different inductors (in blue O-shape coil with polyurethane support, in yellow linear coil and in a green O-shape coil with fiberglass/epoxy resin composite support).

Inductor #	Shots Per Energy														Total Shots	Total Cumulative Energy (kJ)	Average Energy Usage
	5	6	7	8	9	10	11	12	13	14	15	16	17	18			
9	0	0	0	0	0	0	0	0	0	0	0	3	0	0	3	48	16
8	0	0	0	0	0	3	0	0	3	0	0	1	0	0	7	85	12
7	0	0	0	0	0	3	0	0	3	0	0	3	0	0	9	117	13
3	0	0	0	0	0	3	0	0	2	0	0	6	0	0	11	152	14
4	0	0	0	0	0	4	0	0	3	0	0	4	0	0	11	143	13
6	0	0	0	0	0	3	0	0	5	1	0	3	0	0	12	157	13
5	0	1	3	3	5	2	1	0	1	0	0	3	0	0	19	188	10
14	0	0	0	0	0	3	0	0	5	0	0	25	0	0	33	495	15
10	0	0	0	1	0	6	0	0	10	3	0	14	0	0	34	464	14
13	0	0	0	0	0	7	0	8	4	7	0	16	0	1	43	590	14
12	0	0	0	0	0	15	0	0	16	0	0	16	0	0	47	614	13
2	5	11	10	8	6	6	0	0	7	0	0	0	0	0	53	430	8

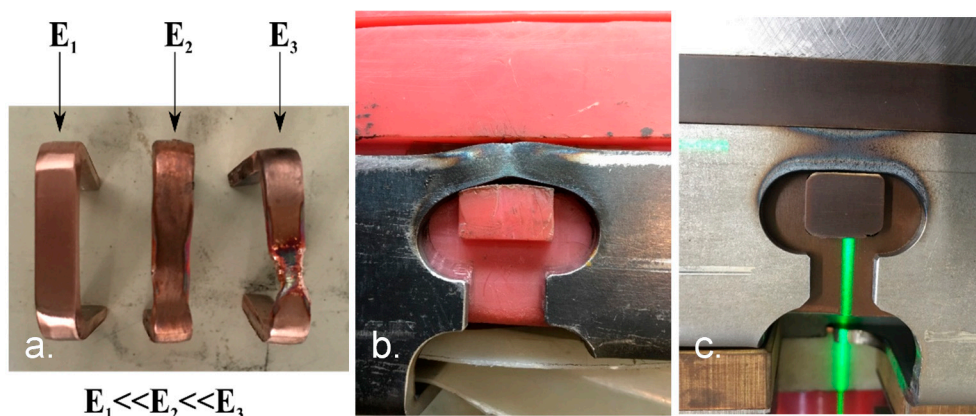**Figure 18.** Effect of different levels of thermo-mechanical stresses for: (**a**) linear coil, (**b**) O-shape coil with PU support, (**c**) O-shape coil with fiberglass/epoxy resin composite support.

4. Conclusions

Electromagnetic pulse welding between similar (Al/Al) and dissimilar metals (Al/Steel) with straight (I-shape) and O-shape coils has been investigated using two different layouts, i.e., straight (MPW) or humped (MPSW) for the lap joints. The conclusions presented herein are relevant to

maximum discharge energies up to 16 kJ using copper and steel coils, and a flyer–parent standoff between 1 and 3 mm. The numerical simulation of straight and O-shape coils using coupled mechanical/thermal/electromagnetic using LS-DYNA 3D Finite Element Method–Boundary Element Method code (FEM-BEM) is employed as an asset to estimate the effect of coil shape on the welding of different alloyed Al–Steel couples. The conclusions of the numerical model are then validated by experimental production and characterization of lap welds in Al/Al, Al/steel couples of interests in automotive industry. The main conclusions can be summarized as follows:

1. Simulation suggests that O-shape coils have higher process efficiency when measured on impact velocity criterion compared to straight (I-shape) coils for identical process parameters (discharge Energy, flyer–parent gap). Irrespective of the coil material, O-shape coils produce higher impact velocities which are propitious to effective welding. The maximum impact velocities of 550 and 900 m/s are, respectively, estimated for straight and O-shape copper coils. Impact velocity increases with standoff linearly for straight coils, contrary to O-shape coils where a velocity plateau seems to shift towards higher standoffs with increasing discharge energy. For instance, the plateau onset point moves from 1.6 to 2.1 mm when discharge energy goes up from 10 to 13 kJ for copper O-shape coil. At 16 kJ, the plateau onset is not observed for copper O-shape coil within the standoff of 2.8 mm;

2. Compared to steel, copper coil is estimated to generate superior impact velocities (900 m/s for copper O-shape coil vs. 710 m/s for steel O-shape coil at 16 kJ). Copper has a higher electrical conductivity—lower joule losses—but lower mechanical resistance than steel. Joule losses in steel coils end up with coil heating and would require cooling to maintain its stiffness in heavy duty applications as in automotive plants. The disadvantage with copper as coil material stem from the fact that coil gets heavy recoil pressure from the outgoing flyer sheet, which significantly reduces the life cycle of coil. Copper coils' lifetime is reduced to a very few welds as the discharge energy increases;

3. The life cycle of the O-shape coil is significantly higher than that of the straight coil and is subject to how the coil is mounted in its holding system. Though reasonable from a theoretical point of view, this requires further study for a quantitative measure;

4. Higher impact velocities with O-shape coil, derived from numerical calculations, are indirectly validated by the possibility of welding additional couple sheets that were not straight coil at the tested discharge energies. For example, 1.4-mm thick 5182 was welded with 5754, DP450, and DC04; 2-mm thick 5182 with 5754, DP450, DC04, and, finally, 6013 with DP1000. As a general rule, thicker and materials with higher mechanical characteristics require superior discharge energies capable of providing higher impact velocities. When the generator has limited disposable energy, O-shape coil is a preferential choice for electromagnetic pulse welding;

5. Quasi-static, dynamic shear tests along with fatigue test results on different sheet combinations attest a higher resistance of the spot welds as fracture occurred outside the welds, mostly around the corners of the welded spots where applied stresses are concentrated.

The investigations reported here are focused on the application of electromagnetic pulses for the sheet metal welding in automotive applications in view of lightweight hybrid tailored structures, like body parts. The results do indicate a viable process approach and feasibility, as reported here.

Author Contributions: Conceptualization, C.K., S.M., G.R.; Methodology, C.K., G.R.; Software, C.K., G.R.; Validation, C.K., S.M., G.R.; Formal Analysis, C.K., S.M., G.R.; Investigation, C.K., G.R.; Resources, C.K., G.R.; Data Curation, C.K., S.M., G.R.; Writing—Original Draft Preparation, C.K., S.M., G.R.; Writing—Review and Editing, C.K., S.M., G.R.; Visualization, C.K., S.M., G.R.; Supervision, G.R.; Project Administration, G.R. All authors have read and agreed to the published version of the manuscript.

Conflicts of Interest: The authors declare no conflict of interest.

References

1. Messler, R.W. *Joining of Materials and Structures: From Pragmatic Process to Enabling Technology*; Butterworth-Heinemann: Burlington, MA, USA, 2004.
2. Grote, K.-H.; Antonsson, E.K. *Springer Handbook of Mechanical Engineering*; Springer Science & Business Media: New York, NY, USA, 2009; Volume 10.
3. Gould, J.E. Joining aluminum sheet in the automotive industry—A 30 year history. *Weld. J.* **2012**, *91*, 23–34.
4. Solomon, H.D. Fundamentals of Weld Solidification. In *Welding, Brazing and Soldering*; ASM International: Novelty, OH, USA, 1993; pp. 45–54. ISBN 978-1-62708-173-3.
5. Cieslak, M.J. Cracking Phenomena Associated With Welding. In *Welding, Brazing and Soldering*; ASM International: Novelty, OH, USA, 1993; pp. 88–96. ISBN 978-1-62708-173-3.
6. Wagner, M.; Jahn, A.; Brenner, B. Innovative joining technologies for multi-material lightweight car body structures. In Proceedings of the International Automotive Body Congress (IABC), Dearborn, MI, USA, 29–30 October 2014; pp. 29–30.
7. Kulkarni, N.; Mishra, R.S.; Yuan, W. *Friction Stir Welding of Dissimilar Alloys and Materials*; Butterworth-Heinemann: Oxford, UK, 2015.
8. Matthew Gilloon, C.G. Remote laser welding boosts production of new Ford Mustang. *Ind. Laser Solut.* **2017**, *32*, 28–31.
9. Agudo, L.; Eyidi, D.; Schmaranzer, C.H.; Arenholz, E.; Jank, N.; Bruckner, J.; Pyzalla, A.R. Intermetallic Fe x Al y-phases in a steel/Al-alloy fusion weld. *J. Mater. Sci.* **2007**, *42*, 4205–4214. [CrossRef]
10. Rathod, M.; Kutsuna, M. Use of pulsed CO_2 laser in laser roll bonding of A5052 aluminium alloy and low carbon steel. *Weld. World* **2006**, *50*, 28–36. [CrossRef]
11. Van der Rest, C.; Jacques, P.J.; Simar, A. On the joining of steel and aluminium by means of a new friction melt bonding process. *Scr. Mater.* **2014**, *77*, 25–28. [CrossRef]
12. Blazynski, T.Z. *Explosive Welding, Forming and Compaction*; Springer Science & Business Media: New Yok, NY, USA, 2012.
13. Daehn, G.S.; Lippold, J.; Liu, D.; Taber, G.; Wang, H. Laser impact welding. In Proceedings of the 5th International Conference on High Speed Forming, Dortmund, Germany, 24–26 April 2012.
14. Vivek, A.; Hansen, S.R.; Liu, B.C.; Daehn, G.S. Vaporizing foil actuator: A tool for collision welding. *J. Mater. Process. Technol.* **2013**, *213*, 2304–2311. [CrossRef]
15. Manoharan, P.; Manogaran, A.P.; Priem, D.; Marya, S.; Racineux, G. State of the art of electromagnetic energy for welding and powder compaction. *Weld. World* **2013**, *57*, 867–878. [CrossRef]
16. Bellmann, J.; Lueg-Althoff, J.; Schulze, S.; Gies, S.; Beyer, E.; Tekkaya, A.E. Measurement and analysis technologies for magnetic pulse welding: Established methods and new strategies. *Adv. Manuf.* **2016**, *4*, 322–339. [CrossRef]
17. Shotri, R.; Racineux, G.; De, A. Magnetic pulse welding of metallic tubes—Experimental investigation and numerical modelling. *Sci. Technol. Weld. Join.* **2020**, *25*, 273–281. [CrossRef]
18. Manogaran, A.P.; Manoharan, P.; Priem, D.; Marya, S.; Racineux, G. Magnetic pulse spot welding of bimetals. *J. Mater. Process. Technol.* **2014**, *214*, 1236–1244. [CrossRef]
19. Manogaran, A.P. Développement du Procédé de Soudage par Point par Implusion Magnétique: Assemblage Hétérogène Al/Fe. Doctoral Dissertation, Ecole centrale de Nantes, Nantes, France, 2013.
20. Marya, M.; Marya, S. Interfacial microstructures and temperatures in aluminium—Copper electromagnetic pulse welds. *Sci. Technol. Weld. Join.* **2004**, *9*, 541–547. [CrossRef]
21. Aizawa, T. Magnetic Pulse Welding of Al/Cu Sheets Using 8-Turn Flat Coil. *J. Light Met. Weld.* **2020**, *58*, 97s–101s.
22. Avettand-Fènoël, M.-N.; Khalil, C.; Taillard, R.; Racineux, G. Effect of steel galvanization on the microstructure and mechanical performances of planar magnetic pulse welds of aluminum and steel. *Metall. Mater. Trans. A* **2018**, *49*, 2721–2738. [CrossRef]
23. Mallick, P.K. *Materials, Design and Manufacturing for Lightweight Vehicles*; Elsevier: Amsterdam, The Netherlands, 2010.

24. Johnson, G.R.; Cook, W.H. A constitutive model and data for metals subjected to large strains, high strain rates and high temperatures. In Proceedings of the 7th International Symposium on Ballistics, The Hague, The Netherlands, 19–21 April 1983; Volume 21, pp. 541–547.

25. Seidt, J.D.; Gilat, A.; Klein, J.A.; Leach, J.R. High strain rate, high temperature constitutive and failure models for EOD impact scenarios. In Proceedings of the SEM Annual Conference & Exposition on Experimental and Applied Mechanics, Springfield, MA, USA, 3–6 June 2007; p. 15.

26. Smerd, R.; Winkler, S.; Salisbury, C.; Worswick, M.; Lloyd, D.; Finn, M. High strain rate tensile testing of automotive aluminum alloy sheet. *Int. J. Impact Eng.* **2005**, *32*, 541–560. [CrossRef]

27. Verleysen, P.; Peirs, J.; Degrieck, J. Experimental study of dynamic fracture in Ti6A14V. In Proceedings of the 4th International Conference on Impact Loading of Lightweight Structures (ICILLS 2014), Cape Town, South Africa, 12–16 January 2014.

28. Burgess, T.J. Electrical resistivity model of metals. In Proceedings of the 4th International Conference on Megagauss Magnetic-Field Generation and Related Topics, Santa Fe, NM, USA, 14–17 July 1986.

29. Hallquist, J.O. *LS-DYNA Theory Manual*; Livermore Soft-Ware Technology Corporation: Livermore, CA, USA, 2006.

30. Mamutov, A.V.; Golovashchenko, S.F.; Mamutov, V.S.; Bonnen, J.J. Modeling of electrohydraulic forming of sheet metal parts. *J. Mater. Process. Technol.* **2015**, *219*, 84–100. [CrossRef]